COMPUTER METHODS IN MATERIALS SCIENCE

2022, vol. 22, no. 1, 31–42
https://doi.org/10.7494/cmms.2022.1.0776

Thermomechanical modeling on the crack initiation of NiTi shape memory alloy

Dongjie Jiang[1], Yao Xiao[2,3]*

[1] School of Aeronautics and Astronautics, Shanghai Jiao Tong University, 200240 Shanghai, China.
[2] School of Mechanical Engineering, Tongji University, 201804 Shanghai, China.
[3] Institute for Advanced Study, Tongji University, 200092 Shanghai, China.

Abstract

The fracture of shape memory alloys is distinct from that of conventional metals, owing to the coexistence and interaction of multiple special features such as martensitic transformation, dislocation-induced plasticity, thermomechanical coupling and others. In this paper, the impact of thermomechanical behavior upon the crack initiation of a NiTi shape memory alloy under Mode I loading is investigated numerically and verified experimentally. A constitutive model incorporating phase transformation, plasticity and thermomechanical coupling is established. Via backward Euler integration and finite-element implementation, the longitudinal strain, martensite volume fraction and temperature field in the vicinity of the crack tip are furnished. The effects of grain size and loading rate on *J*-integral are revealed. The grain size dependence of crack initiation is non-monotonic. For the samples with grain sizes of 1500 nm, 18 nm and 10 nm, the shielding effect takes place in front of the crack. Additionally, the anti-shielding effect is detected for samples with grain sizes of 80 nm and 42 nm. The parametric study shows that loading rate imposes limited influence on *J*-integral, which is attributed to a small scale transformation. The decrement of yield stress and the increment of transformation hardening modulus can alleviate the anti-shielding effect and arouse the shielding effect upon crack initiation. The presented results shed light on the design and fabrication of high toughness phase transformable materials.

Keywords: shape memory alloy, martensitic transformation, crack initiation, thermomechanical coupling

1. Introduction

Shape memory alloys (SMAs) are unique materials characterized by reversible martensitic transformation. An emerging application of SMA is solid-state cooling based on the elastocaloric effect (eCE), i.e. a temperature change associated with an applied load (Imran & Zhang, 2020). Among all classes of SMAs, superelastic NiTis possess high adiabatic temperature change (~25 K) and outstanding recoverable strain (~7%). Since flaws are unavoidable during processing and fabrication, thermomechanically coupled fracture toughness is an essential property influencing the service under cyclic loading (Jape et al., 2021; LePage et al., 2021; Shuai & Xiao, 2020; Xu et al., 2021; Zhang et al., 2019).

Considerable experiments have been carried out to explore the fracture behavior of NiTis. Daly et al. (2007) employed in situ digital image correlation (DIC) to map the strain field of a cracked NiTi. Robertson et al. (2007), Daymond et al. (2007), Gollerthan et al. (2009) and Ungár et al. (2017) studied the strain field, the phase evolution and the grain orientation ahead of the crack via synchrotron X-ray diffraction. The transformed region and plastic region were identified in the vicinity of the crack tip. Maletta et al. (2014)

*Corresponding author: xiaoy10@tongji.edu.cn
ORCID ID's: 0000-0001-9539-0440 (D. Jiang), 0000-0003-3011-8408 (Y. Xiao)

and You et al. (2019) utilized infrared thermography and DIC to capture the thermomechanical behavior of a single-edge cracked NiTi. An inhomogeneous temperature near the crack tip was observed, implying that thermomechanical coupling should be carefully treated to predict the fracture behavior. In order to have an in-depth understanding of the toughening mechanism of NiTis, several computational studies have been conducted based on analytical expression and finite-element approach. Baxevanis et al. (2013) investigated numerically the stable crack growth in a superelastic NiTi. The effect of maximum transformation strain, transformation hardening, mismatch of Young's moduli of the two phases, and the ambient temperature were analyzed. Hazar et al. (2015) studied the influence of martensite reorientation on the steady-state crack growth of SMAs. The shielding effect was discernable at the crack tip under both plane strain and plane stress conditions. By suppressing martensitic transformation at temperatures above martensite desist temperature, Haghgouyan et al. (2016) studied the critical stress intensity factor (K_{IC}) of a NiTi under Mode I loading, and they claimed that transformable material is tougher than transformation-suppressed material due to transformation toughening. Ardakani et al. (2015, 2016) simulated crack propagation with a thermomechanically coupled extended finite-element method, and they argued that the size of the transformation zone decreases with loading rate. Mutlu et al. (2020) showed that K_{IC} for crack initiation increases with loading rate, which is ascribed to the joint effect of martensitic transformation and energy dissipation. However, Baxevanis et al. (2014) anticipated the loss of transformation toughening when the NiTi is loaded under adiabatic conditions. Therefore, the thermomechanically coupled fracture behavior of NiTis is complicated and a fundamental study is necessary for a better understanding of its toughening mechanism.

In this work, the thermomechanical behavior upon the crack initiation of a NiTi under Mode I loading is studied numerically. A constitutive model involving martensitic transformation, plasticity and thermomechanical coupling is developed. Via backward Euler integration and finite-element implementation, the longitudinal strain, martensite volume fraction and temperature contour of the cracked samples are analyzed. The effects of loading rate, grain size and other material parameters on the *J*-integral are scrutinized. The novelties of the work are twofold. On the one hand, our simulation verified that loading rate has a limited effect on the crack initiation of a NiTi, and we clarified that the rate insensitivity of crack initiation is attributed to "small scale transformation". On the other hand, the non-monotonic grain size dependence on crack initiation was disclosed. The samples with grain sizes of 1500 nm, 18 nm and 10 nm demonstrate the shielding effect, while those with grain sizes of 80 nm and 42 nm exhibit the anti--shielding effect. The present results will shed light on the design and fabrication of high toughness NiTis and other phase transformable materials.

2. Constitutive model

2.1. Definition of strain and energy

Experimental observation indicates that NiTis undergo elastic deformation, martensitic transformation and plastic deformation near the crack tip (Daly et al., 2007). Therefore, the total strain ε_{ij} is decomposed into elastic strain ε_{ij}^{e}, transformation strain ε_{ij}^{t} and plastic strain ε_{ij}^{p}:

$$\varepsilon_{ij} = \varepsilon_{ij}^{e} + \varepsilon_{ij}^{t} + \varepsilon_{ij}^{p} \tag{1}$$

The specific Gibbs energy (G) is divided into the thermoelastic energies of austenite and martensite (G^A and G^M) and the specific energy originating from martensitic transformation (G^m):

$$G = (1-\xi)G^{A}(\sigma_{ij},\theta) + \xi G^{M}(\sigma_{ij},\theta) + G^{m} \tag{2}$$

where ξ is the martensite volume fraction, which is proportional to macroscopic transformation strain (Xiao & Jiang, 2020a, 2020b):

$$\xi = \frac{\overline{\varepsilon}^{t}}{\varepsilon_{\max}^{t}} \tag{3}$$

where $\varepsilon_{\max}^{t}$ is the maximum transformation strain and $\overline{\varepsilon}^{t}$ is the equivalent transformation strain. G^A and G^M are expressed as:

$$\begin{aligned} G^{X} &= -\frac{1}{2}S_{ijkl}^{X}\sigma_{ij}\sigma_{kl} + u_{0}^{X} - \theta s_{0}^{X} + \\ & c\left(\theta - \theta_{0} - \theta\ln\frac{\theta}{\theta_{0}}\right) \quad X = A, M \end{aligned} \tag{4}$$

where S_{ijkl}^{X} is the elastic compliance. u_0^X and s_0^X are specific internal energy and specific entropy at balance temperature θ_0, respectively. c is the specific heat capacity of both phases. A and M represent austenite and martensite, respectively. The effective elastic compliance is defined as:

$$S_{ijkl} = (1-\xi)S_{ijkl}^{A} + \xi S_{ijkl}^{M} \tag{5}$$

The elastic property of each phase is assumed to be isotropic:

$$S_{ijkl}^{X}=\frac{1}{E_X}\left[(1+\nu)I_{ijkl}-\nu\delta_{ij}\delta_{kl}\right]\quad X=A,M \tag{6}$$

where I_{ijkl} is the fourth-order identity tensor, E_X is the elastic modulus, and v is Poisson's ratio. G^m is defined as (Lagoudas et al., 2012):

$$G^m=G^h+G^{ind}-\sigma_{ij}(\varepsilon_{ij}-\varepsilon_{ij}^e) \tag{7}$$

where G^h is the energy caused by transformation hardening, and G^{ind} is the indicator energy forcing $\bar{\varepsilon}^t$ consistently less than $\varepsilon_{\max}^t$. In light of Yu et al. (2018), G^h is expressed as:

$$G^h=\frac{1}{2}H_1(\bar{\varepsilon}^t)^2 \tag{8}$$

where H_1 is the material parameter reflecting the transformation hardening modulus. The energy G^{ind} is proposed to make $\bar{\varepsilon}^t$ consistently less than $\varepsilon_{\max}^t$ (Xiao & Jiang, 2020a):

$$G^{ind}=H_2\times \begin{cases} 0 & 0\le\bar{\varepsilon}^t<\varepsilon_{\max}^t-d \\ d^2\left(0.5\zeta^5-0.5\zeta^6+\dfrac{\zeta^7}{7}\right) & \varepsilon_{\max}^t-d\le\bar{\varepsilon}^t\le\varepsilon_{\max}^t \\ d\left[\dfrac{d}{7}+\dfrac{(\bar{\varepsilon}^t-\varepsilon_{\max}^t)}{2}\right]+\dfrac{(\bar{\varepsilon}^t-\varepsilon_{\max}^t)^2}{2} & \bar{\varepsilon}^t\ge\varepsilon_{\max}^t \end{cases} \tag{9}$$

where $\zeta=\left(\bar{\varepsilon}^t-\varepsilon_{\max}^t+d\right)/d$. H_2 is a large constant and d is a small constant (i.e. $H_2=20{,}000$ GPa and $d=0.0001$).

2.2. Thermodynamic framework

Allowing for the second law of thermodynamics, the dissipation should be non-negative:

$$\Gamma=-\dot{\sigma}_{ij}\varepsilon_{ij}-s\dot{\theta}-\dot{G}-\frac{\mathbf{q}\cdot\nabla\theta}{\theta}\ge 0 \tag{10}$$

where s is entropy density, $\mathbf{q}$ is heat flux. Substituting Equations (1)–(7) into Equation (10), we arrive at:

$$\begin{aligned}\Gamma=&(S_{ijkl}\sigma_{ij}-\varepsilon_{kl}^e)\dot{\sigma}_{kl}+\\&\left[\sigma_{ij}-(-\Delta u_0+\Delta s_0\theta)\frac{\partial\xi}{\partial\varepsilon_{ij}^t}+\right.\\&\left.\frac{1}{2}\sigma_{pq}\frac{\partial S_{pqrs}}{\partial\varepsilon_{ij}^t}\sigma_{rs}-\frac{\partial(G^h+G^{ind})}{\partial\varepsilon_{ij}^t}\right]\dot{\varepsilon}_{ij}^t+\\&\sigma_{ij}\dot{\varepsilon}_{ij}^p-\left(s+\Delta s_0\xi-s_0^A-c\ln\frac{\theta}{\theta_0}\right)\dot{\theta}+\frac{k:(\nabla\theta\otimes\nabla\theta)}{\theta}\ge 0\end{aligned} \tag{11}$$

where $\Delta u_0=u_0^A-u_0^M$ and $\Delta s_0=s_0^A-s_0^M$. The following definitions are proposed for the sake of simplicity:

$$\sigma_{ij}=(S_{ijkl})^{-1}\varepsilon_{kl}^e \tag{12}$$

$$s=s_0^A-\Delta s_0\xi+c\ln\frac{\theta}{\theta_0} \tag{13}$$

$$\sigma_{ij}^B=\frac{\partial(G^h+G^{ind})}{\partial\varepsilon_{ij}^t}+(-\Delta u_0+\Delta s_0\theta)\frac{\partial\xi}{\partial\varepsilon_{ij}^t} \tag{14}$$

$$\bar{\sigma}_{ij}=\frac{1}{2}\sigma_{pq}\frac{\partial S_{pqrs}}{\partial\varepsilon_{ij}^t}\sigma_{rs} \tag{15}$$

$$\hat{\sigma}_{ij}=\sigma_{ij}-\sigma_{ij}^B+\bar{\sigma}_{ij} \tag{16}$$

Substituting Equations (8) and (9) into Equation (14), we get:

$$\sigma_{ij}^B=\sigma_B\frac{\partial\bar{\varepsilon}^t}{\partial\varepsilon_{ij}^t} \tag{17}$$

$$\sigma_B=\sigma_s+\beta(\theta-\theta_r)+H_1\bar{\varepsilon}^t+H_2\begin{cases}0 & 0\le\bar{\varepsilon}^t<\varepsilon_{\max}^t-d\\ d(2.5\zeta^4-3\zeta^5+\zeta^6) & \varepsilon_{\max}^t-d\le\bar{\varepsilon}^t\le\varepsilon_{\max}^t\\ \dfrac{d}{2}+\bar{\varepsilon}^t-\varepsilon_{\max}^t & \bar{\varepsilon}^t\ge\varepsilon_{\max}^t\end{cases} \tag{18}$$

where σ_B is the back stress, θ_r is the ambient temperature, $\beta=\Delta s_0/\varepsilon_{\max}^t$ controls the temperature dependence of the back stress, and $\sigma_s=-\Delta u_0+\Delta s_0\theta_r/\varepsilon_{\max}^t$ reflects the back stress at θ_r.

2.3. Transformation and yielding criteria

The transformation surface is proposed to be J_2-type:

$$\Phi^t=\frac{3}{2}\hat{s}_{ij}\hat{s}_{ij}-\sigma_0^2 \tag{19}$$

where $\hat{s}_{ij}$ represents the deviator of $\hat{\sigma}_{ij}$, and σ_0 is the size of the transformation surface. J_2 isotropic hardening is adopted to describe the yielding of the material:

$$\Phi^p=\frac{3}{2}s_{ij}s_{ij}-\sigma_p^2 \tag{20}$$

where s_{ij} is the deviator of σ_{ij}, and σ_p is the yield strength that hardens linearly with plastic deformation:

$$\sigma_p=\sigma_p^{ini}+H_p\bar{\varepsilon}^p \tag{21}$$

where H_p is the material parameter reflecting the hardening modulus caused by plasticity, $\bar{\varepsilon}^p$ is the equivalent plastic strain, and σ_p^{ini} is the initial yield stress when $\bar{\varepsilon}^p=0$. The postulate of maximum dissipation

requires that transformation/plastic strain increment should be normal to the transformation/yielding surface:

$$\dot{\varepsilon}_{ij}^{t} = \lambda^{t} \frac{\partial \Phi^{t}}{\partial \hat{\sigma}_{ij}} \tag{22}$$

$$\dot{\varepsilon}_{ij}^{p} = \lambda^{p} \frac{\partial \Phi^{p}}{\partial \sigma_{ij}} \tag{23}$$

where λ^t and λ^p are non-negative multipliers determined by consistency conditions.

2.4. Heat equilibrium equation

The first law of thermodynamics yields:

$$\dot{U} = \sigma_{ij}\dot{\varepsilon}_{ij} - \nabla \cdot \mathbf{q} \tag{24}$$

The definition of Gibbs free energy leads to:

$$G = U - \sigma_{ij}\varepsilon_{ij} - s\theta \tag{25}$$

Given Equations (10), (24) and (25), we get the heat equilibrium equation:

$$c\dot{\theta} - k\nabla \cdot \nabla\theta = \hat{\sigma}_{ij}\dot{\varepsilon}_{ij}^{t} + \sigma_{ij}\dot{\varepsilon}_{ij}^{p} + \beta\varepsilon_{\max}^{t}\theta\dot{\xi} \tag{26}$$

where k is the isotropic heat conductivity coefficient.

3. Finite-element implementation

3.1. Numerical model

Via backward Euler integration, the constitutive model is implemented into Abaqus UMAT implicitly. The geometry of the sample is shown in Figure 1. The numerical sample with the same geometry is created in the Part Module of Abaqus and then discretized by 8-node thermally coupled brick elements (C3D8T) in the Mesh Module. As shown in Figure 1, the in-plane size of the elements out of the crack tip region (shown as the inset) is 1 mm and the mesh is refined around the crack tip with the element size of 0.025 mm, which is sufficient to get accurate solution around the crack tip (Mutlu et al., 2020).

In the Step Module of Abaqus, a coupled temperature-displacement step is created in which the inertia is neglected, but the thermal process is transient. The boundary conditions and initial temperature are defined in the Load Module. In order to reproduce the experimental setup (Ahadi & Sun, 2016), the vertical displacement of the upper hole is prescribed, in-plane rotation of two holes is allowed, while the other degrees of freedom of two holes are pinned. The initial temperature of the sample is equal to the ambient temperature (θ_r = 293 K). The heat transfer between the testing machine and the sample is modelled as the heat conduction via boundary sections of two holes, i.e., the temperature on the circumferential surfaces of the two holes is kept at the initial temperature. The heat transfer between the sample and the ambient is simplified as heat convection through the lateral surfaces. The temperature of the heat sink for conduction and convection is fixed at θ_r. The heat convection between the lateral surfaces and the ambient is defined in the Interaction Module.

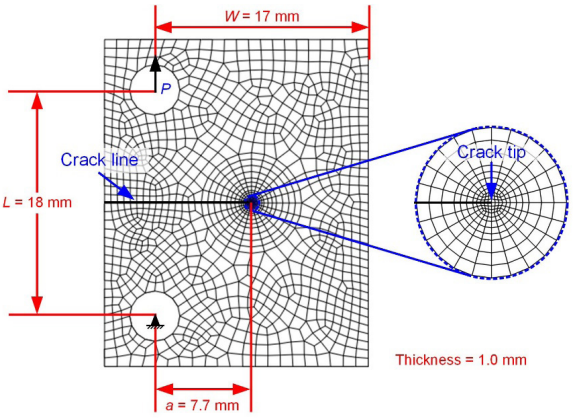

Fig. 1. The geometry and the mesh of the numerical sample

3.2. Parameter calibration

The proposed model is verified by the experiments performed by Ahadi & Sun (2016). The grain size (GS) ranges from 10 nm to 1500 nm. The elastic moduli of austenite and martensite (E_A and E_M) are calibrated by the elastic behavior of austenite and martensite, respectively. Poisson's ratio (ν) is set as 0.3. Heat capacity (c), heat conductivity coefficient (k) and heat convection coefficient (h_{air}) are set as 3.2 × 10^6 J/(m^3·K), 18 W/(m·K) and 6.5 W/(m^2·K), respectively (Xiao & Jiang, 2020a).

$\varepsilon_{\max}^{t}$ is assessed by the spanning of the stress plateau from the isothermal stress-strain response. σ_s is calibrated by the transformation stress at θ_r. β has been reported by Ahadi & Sun (2013). σ_0 is determined by half of the stress hysteresis of the isothermal stress-strain response. H_1 is evaluated by the transformation hardening modulus during martensitic transformation. σ_p^{ini} equals to the stress value at the intersection of extrapolated plastic branch and extrapolated elastic branch of martensite. H_p is calibrated by the hardening modulus in the course of plastic deformation. Material parameters are summarized in Table 1. The calibrated mechanical response under isothermal uniaxial loading is verified with the experimental result in Figure 2.

Table 1. Mechanical parameters of NiTi

	Sample A (GS = 1500 nm)	Sample B (GS = 80 nm)	Sample C (GS = 42 nm)	Sample D (GS = 18 nm)	Sample E (GS = 10 nm)
E_A [GPa]	63	63	36	40	52
E_M [GPa]	15	32	25.5	30	41
v	0.3	0.3	0.3	0.3	0.3
β [MPa/K]	6.5	6.25	5.8	3.54	0.3
σ_s[MPa]	235	285	340	260	260
σ_0[MPa]	155	145	130	170	230
σ_p^{ini} [MPa]	500	1300	1450	1350	1220
H_1 [GPa]	1	2	8	68	380
H_p [GPa]	3	9	9	9	9
$\varepsilon_{\max}^t$	0.05	0.045	0.025	0.013	0.0036

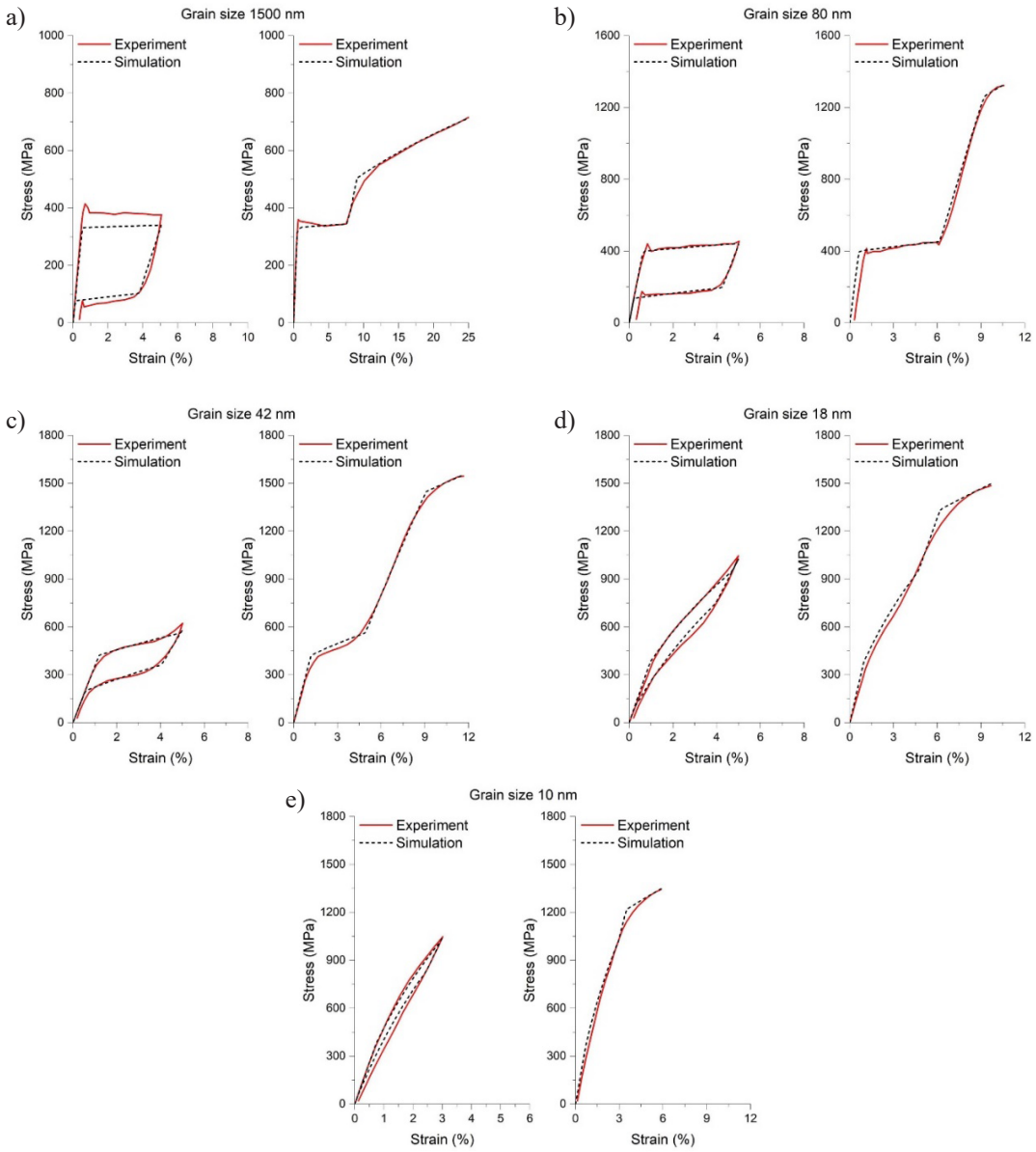

Fig. 2. Calibrated isothermal response under uniaxial loading (the experimental results are adopted from Ahadi & Sun, 2016): a) sample A (GS = 1500 nm); b) sample B (GS = 80 nm); c) sample C (GS = 42 nm); d) sample D (GS = 18 nm); e) sample E (GS = 10 nm)

4. Verification

Analogously to the experimental setup, the loading rate is prescribed as 5 mm/min. The applied force and the longitudinal strain (strain component parallel to the loading direction) are designated as P and ε_{22}. The fracture load (P_{max}) is adopted from Ahadi & Sun (2016). Simulated contour plots of longitudinal strain, martensite volume fraction and temperature at various P are depicted in Figure 3.

The strain field is featured with two inclined lobes, and they grow as loading proceeds while the shape remains unchanged. Martensitic transformation concentrates ahead of the crack tip. We can identify the saturation region (fully martensite), the untransformed region (fully austenite) and the partially transformed region (mixture of austenite and martensite). For GS = 1500 nm, the diameters of the saturation region and partially transformed region at P_{max} are about 0.9 mm and 3.6 mm. When GS is reduced to 42 nm, the diameter of the transformation zone at P_{max} shrinks to 2 mm. When GS is further reduced to 18 nm and 10 nm, the diameter of the transformation zone decreases to 0.7 mm, and the saturation region is nearly undiscernible. Martensitic transformation and plastic deformation result in the release of transformation latent heat and mechanical dissipation, so the NiTi exhibits rate dependence when the heat transfer is limited. The maximal temperature rise in front of the crack tip drops monotonically from 4 K to 0.05 K as GS decreases from 1500 nm to 10 nm, which is consistent with the experimental results (Ahadi & Sun, 2016). This phenomenon can be attributable to the reduction of latent heat and the drop of transformation stress hysteresis in nanocrystalline NiTis.

J-integral is calculated along the concentric circular paths with the center at the crack tip. For a homogeneous and non-dissipative material, J-integral is path independent. However, in the NiTi, J-integral demonstrates path dependence owing to nonlinear and inelastic deformation mechanisms, i.e. martensitic transformation and plasticity. Accordingly, it is vital to distinguish the crack tip J-integral (J^{tip}) and far field J-integral (J^{far}). The evolution of J^{tip} and J^{far} is illustrated in Figure 4. We can see that although the relative magnitude of J-integral varies pronouncedly as applied force increases, J-integral of Sample E (GS = 10 nm) remains rather low.

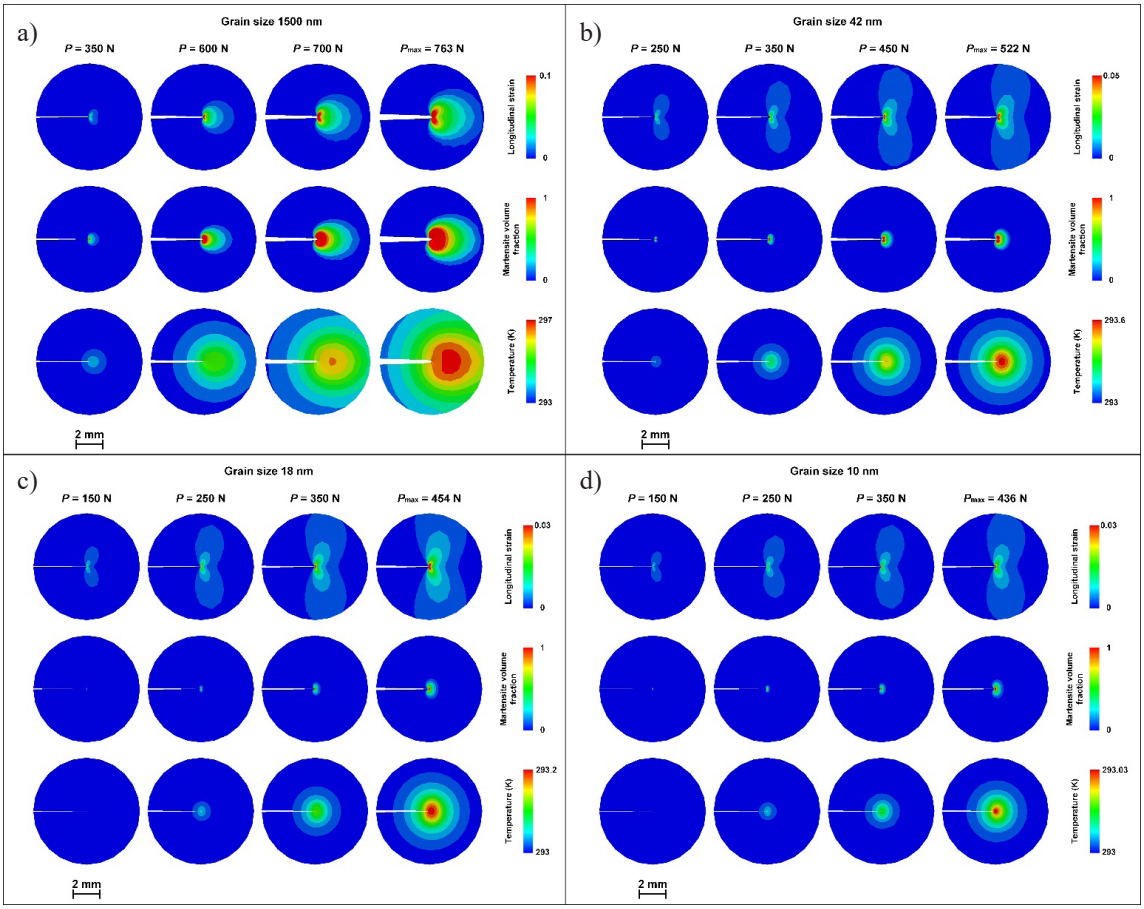

Fig. 3. Simulated contour plots of longitudinal strain (the first row), martensite volume fraction (the second row) and temperature (the third row) in an enlarged circular vision around the crack tip (the scale bar for all the snapshots is 2 mm): a) sample A (GS = 1500 nm); b) sample C (GS = 42 nm); c) sample D (GS = 18 nm); d) sample E (GS = 10 nm)

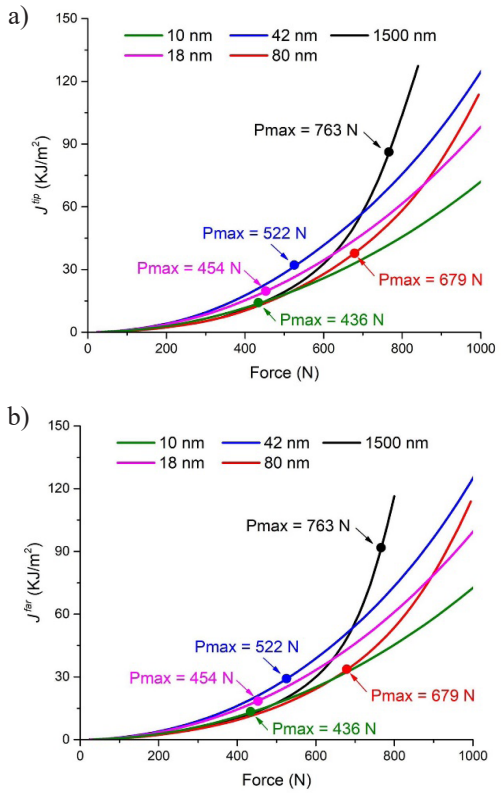

Fig. 4. The evolution of J^{tip} and J^{far} with respect to grain size and applied force. *J*-integral at the fracture load is highlighted with circle

In order to reveal the grain size dependence of the crack initiation in the NiTi, the path dependence of *J*-integral at various applied forces is depicted in Figure 5. For GS = 1500 nm, 18 nm and 10 nm, J^{tip} is lower than J^{far}, leading to the shielding effect. For GS = 80 nm and 42 nm, *J*-integral within the radius of 0.5 mm is higher than J^{far}, so the samples exhibit an anti-shielding effect, which promotes crack initiation. Lepage et al. (2018) examined the fatigue performance of the same samples used in the present study. They found that the samples with GS of 80 nm and 42 nm possess the fastest crack growth rates and the largest crack opening displacements, which strongly corroborates the present numerical results. As illustrated qualitatively by Jiang & Landis (2016), the difference between J^{tip} and J^{far} is attributable to the competition between plasticity and transformation. Plasticity tends to enhance the shielding effect, i.e. inducing a J^{tip} lower than J^{far}, and transformation produces the converse effect. Quantitatively, the sharp contrast of the crack initiation behavior originates from the variation of σ_p^{ini} and H_1, which will be analyzed in Section 5.2. Studies on different martensitic transformations in SMAs like those investigated in Roy (2020) or phase transformations under extreme conditions, e.g., see Javanbakht (2021) and the mechanism of associated micro-crack growth will be performed in future work.

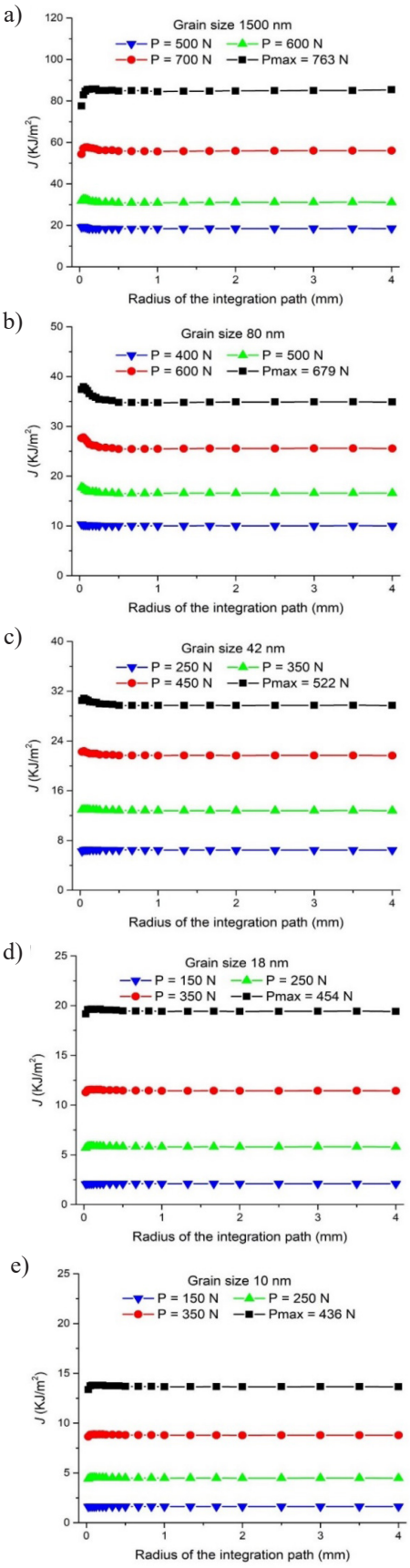

Fig. 5. The evolution of *J*-integral at various applied forces (the loading rate is 5 mm/min): a) sample A (GS = 1500 nm); b) sample B (GS = 80 nm); c) sample C (GS = 42 nm); d) sample D (GS = 18 nm); e) sample E (GS = 10 nm)

5. Discussion

In order to elucidate the effect of thermomechanical coupling, martensitic transformation and plasticity on the fracture initiation of the NiTi, an additional parametric study is conducted in this section. Various material parameters and loading conditions are assigned to the numerical model.

5.1. Effect of loading rate on crack initiation

The thermomechanical responses of the cracked samples deformed isothermally, deformed at 0.5 mm/min, and deformed at 50 mm/min are simulated. The criteria for the crack initiation assumed that J^{tip} equals to the critical value (G_{IC}). In Section 4, G_{IC} can be readily calculated when the numerical sample is subjected to fracture load ($P_{\max}$). The simulation results when crack initiates ($J^{tip} = G_{IC}$) are shown in Figures 6 and 7.

As the loading rate elevates, NiTi is manifested as transformation hardening (due to Clausius–Clapeyron relation) and variation of sample temperature (controlled by the heat transfer). Figure 6 demonstrates that the loading rate imposes a neglectable influence on the distribution of longitudinal strain and martensite volume fraction at the crack tip. When crack initiates ($J^{tip} = G_{IC}$), the maximal temperature in front of the crack is designated as $T_{\max}$. As shown in Figure 7, $T_{\max}$ keeps almost unchanged because the latent heat of the samples with GS of 10 nm and 18 nm is small. When GS $\geq$ 42 nm, $T_{\max}$ increases notably with increasing loading rate. However, for all the samples, when crack initiates, J^{far} varies little whatever strain rate because the size of the transformation zone is much smaller than the sample size, i.e. small scale transformation.

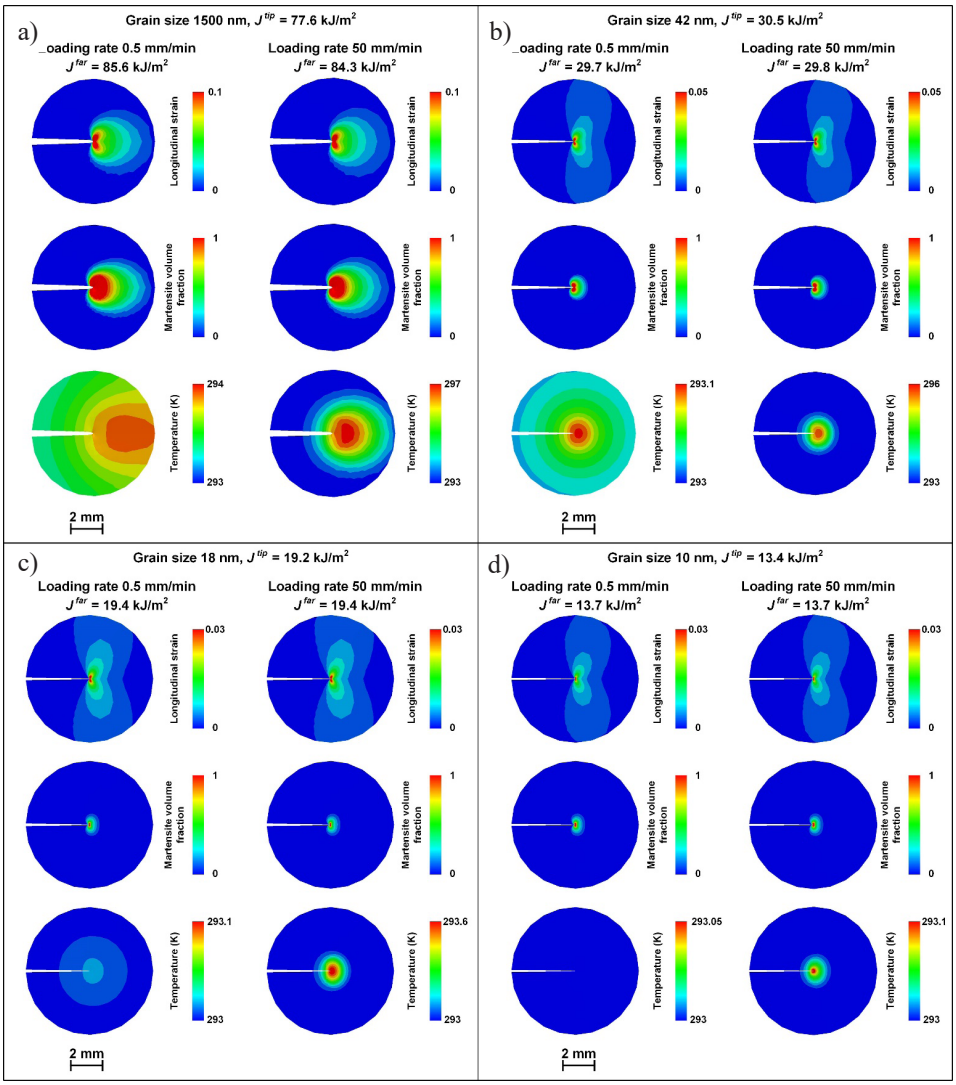

Fig. 6. Simulated contour plots of longitudinal strain, martensite volume fraction and temperature when critical *J*-integral is reached at the crack tip. The loading rates are 0.5 mm/min and 50 mm/min (the scale bar for all the snapshots is 2 mm): a) sample A (GS = 1500 nm); b) sample C (GS = 42 nm); c) sample D (GS = 18 nm); d) sample E (GS = 10 nm)

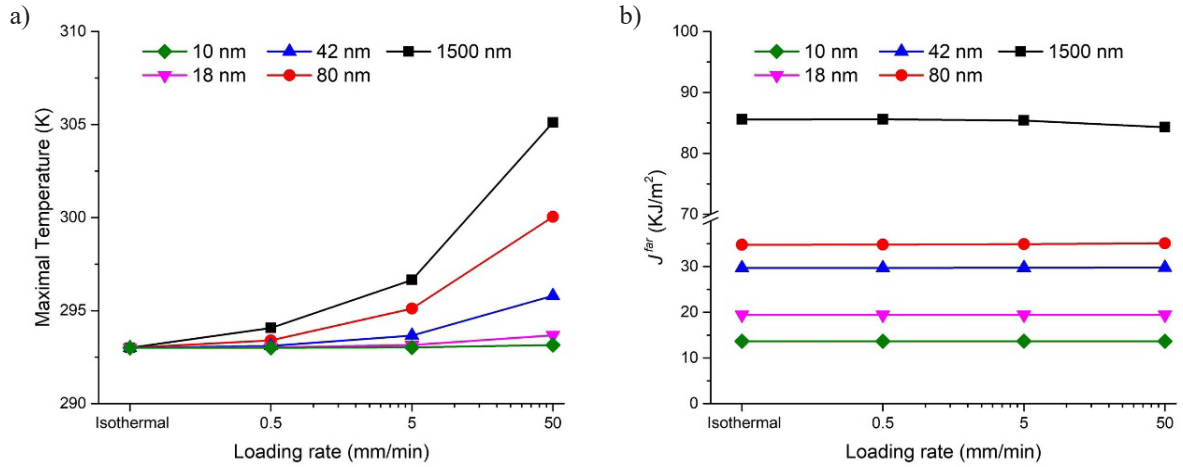

Fig. 7. The effects of loading rate and grain size on maximal temperature in front of the crack (a) and far field *J*-integral when critical *J*-integral is reached at the crack tip (b)

5.2. Effect of plasticity and martensitic transformation on crack initiation

In this subsection, primary attention is paid to Sample B (GS = 80 nm) that demonstrates an evident anti-shielding effect. The numerical results when crack initiates ($J^{tip} = G_{IC}$) are recorded in Figure 8. The effect of plasticity on crack initiation is studied by varying the initial yield stress (σ_p^{ini}) while keeping the other material parameters unaltered. Figure 8a shows that the reduction of σ_p^{ini} will leads to the increment of J^{far}. Similarly, the effect of martensitic transformation on *J*-integral is explored by varying transformation hardening modulus (H_1) while keeping the other material parameters unchanged. In Figure 8b, one can see that the increment of H_1 results in a notable increment of J^{far}. To sum up, numerical results indicate that reducing σ_p^{ini} and increasing H_1 will alleviate the anti-shielding effect and enhance the shielding effect.

Compared with adjusting yield stress, transformation hardening can be realized more easily, e.g. by cold work, grain refinement and thermomechanical cycling (Ahadi & Sun, 2013, 2014, 2016), so transformation hardening is a feasible and appealing approach to improve the fracture toughness of NiTis in the engineering community.

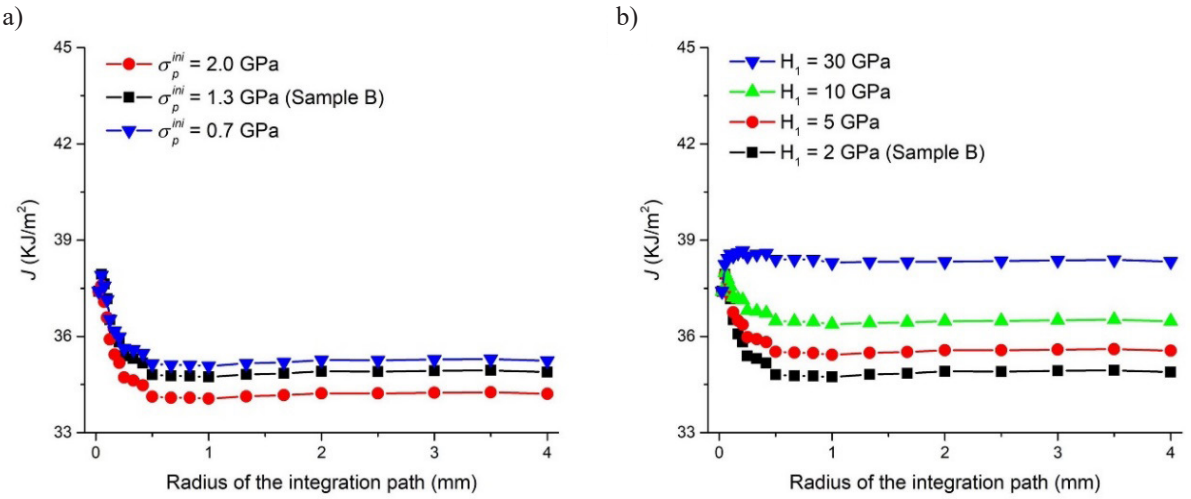

Fig. 8. The evolution of *J*-integral in Sample B (GS = 80 nm) when critical *J*-integral is reached at the crack tip. The loading rate is 5 mm/min. The initial yield stress (σ_p^{ini}) (a) is modified while the other parameters are fixed. Transformation hardening modulus (H_1) (b) is modified while the other parameters are fixed

6. Conclusions

In the present study, the thermomechanical behavior of a single-edge cracked NiTi shape memory alloy under Mode I loading is studied numerically. The constitutive model including martensitic transformation, plasticity and thermomechanical coupling is established. Via finite-element simulation, the longitudinal strain, martensite volume fraction and temperature field in the vicinity of the crack tip are furnished. The major conclusions to be drawn are as follows:

- Martensitic transformation concentrates ahead of the crack tip, and it is suppressed in nanocrystalline NiTis. For the sample with a grain size (GS) of 1500 nm, the diameter of the transformation zone at the fracture load (P_{max}) is about 3.6 mm. When GS is reduced to 42 nm, the diameter of the transformation zone at P_{max} shrinks to 2 mm. If GS is further reduced to 18 nm and 10 nm, the diameter of the transformation region at P_{max} is decreased below 1 mm.
- For GS = 1500 nm, 18 nm and 10 nm, the crack tip *J*-integral (J^{tip}) is lower than far field *J*-integral (J^{far}), leading to the shielding effect. For GS = 80 nm and 42 nm, *J*-integral within the radius of 0.5 mm is higher than J^{far}, so an anti-shielding effect occurs, which promotes crack initiation.
- Loading rate imposes a limited effect on the crack initiation of NiTis. Although the temperature variation in front of the crack increases notably with increasing loading rate for the samples with GS ≥ 42 nm, J^{far} differs slightly owing to "small scale transformation".
- The decrement of yield stress and the increment of transformation hardening modulus alleviate the anti-shielding effect and enhance the shielding effect, which can improve the fracture toughness of NiTis and other phase transformable materials.

Acknowledgments

Yao Xiao acknowledges the support of the Shanghai Sailing Program and the Fundamental Research Funds for the Central Universities. Dongjie Jiang is sponsored by the National Natural Science Foundation of China (Grant No. 11902195).

References

Ahadi, A., & Sun, Q. (2013). Stress hysteresis and temperature dependence of phase transition stress in nanostructured NiTi–Effects of grain size. *Applied Physics Letters*, *103*(2), 021902.

Ahadi, A., & Sun, Q. (2014). Effects of grain size on the rate-dependent thermomechanical responses of nanostructured superelastic NiTi. *Acta Materialia*, *76*, 186–197.

Ahadi, A., & Sun, Q. (2016). Grain size dependence of fracture toughness and crack-growth resistance of superelastic NiTi. *Scripta Materialia*, *113*, 171–175.

Ardakani, S.H., Ahmadian, H., & Mohammadi, S. (2015). Thermo-mechanically coupled fracture analysis of shape memory alloys using the extended finite element method. *Smart Materials and Structures*, *24*(4), 045031.

Ardakani, S.H., Afshar, A., & Mohammadi, S. (2016). Numerical study of thermo-mechanical coupling effects on crack tip fields of mixed-mode fracture in pseudoelastic shape memory alloys. *International Journal of Solids Structures*, *81*, 160–178.

Baxevanis, T., Parrinello, A.F., & Lagoudas, D.C. (2013). On the fracture toughness enhancement due to stress-induced phase transformation in shape memory alloys. *International Journal of Plasticity*, *50*, 158–169.

Baxevanis, T., Landis, C.M., & Lagoudas, D.C. (2014). On the effect of latent heat on the fracture toughness of pseudoelastic shape memory alloys. *Journal of Applied Mechanics*, *81*(10), 101006.

Daly, S., Miller, A., Ravichandran, G., & Bhattacharya, K. (2007). Experimental investigation of crack initiation in thin sheets of nitinol. *Acta Materialia*, *55*(18), 6322–6330.

Daymond, M.R., Young, M.L., Almer, J.D., & Dunand, D.C. (2007). Strain and texture evolution during mechanical loading of a crack tip in martensitic shape-memory NiTi. *Acta Materialia*, *55*(11), 3929–3942.

Gollerthan, S., Young, M.L., Baruj, A., Frenzel, J., Schmahl, W.W., & Eggeler, G. (2009). Fracture mechanics and microstructure in NiTi shape memory alloys. *Acta Materialia*, *57*(4), 1015–1025.

Haghgouyan, B., Shafaghi, N., Aydıner, C.C., & Anlas, G. (2016). Experimental and computational investigation of the effect of phase transformation on fracture parameters of an SMA. *Smart Materials and Structures*, *25*(7), 075010.

Hazar, S., Zaki, W., Moumni, Z., & Anlas, G. (2015). Modeling of steady-state crack growth in shape memory alloys using a stationary method. *International Journal of Plasticity*, *67*, 26–38.

Imran, M., & Zhang, X. (2020). Recent developments on the cyclic stability in elastocaloric materials. *Materials & Design*, *195*, 109030.

Jape, S., Young, B., Haghgouyan, B., Hayrettin, C., Baxevanis, T., Lagoudas, D.C., & Karaman, I. (2021). Actuation-Induced stable crack growth in near-equiatomic nickel-titanium shape memory alloys: Experimental and numerical analysis. *International Journal of Solids Structures*, *221*, 165–179.

Javanbakht, M. (2021). High pressure phase evolution under hydrostatic pressure in a single imperfect crystal due to nanovoids. *Materialia*, *20*, 101199.

Jiang, D., & Landis, C.M. (2016). A constitutive model for isothermal pseudoelasticity coupled with plasticity. *Shape Memory and Superelasticity*, *2*(4), 360–370.

Lagoudas, D.C., Hartl, D., Chemisky, Y., Machado, L., & Popov, P. (2012). Constitutive model for the numerical analysis of phase transformation in polycrystalline shape memory alloys. *International Journal of Plasticity*, *32–33*, 155–183.

LePage, W.S., Ahadi, A., Lenthe, W.C., Sun, Q.P., Pollock, T.M., Shaw, J.A., & Daly, S.H. (2018). Grain size effects on NiTi shape memory alloy fatigue crack growth. *Journal of Materials Research*, *33*(2), 91–107.

LePage, W.S., Shaw, J.A., & Daly, S.H. (2021). Effects of texture on the functional and structural fatigue of a NiTi shape memory alloy. *International Journal of Solids Structures*, *221*, 150–164.

Maletta, C., Bruno, L., Corigliano, P., Crupi, V., & Guglielmino, E. (2014). Crack-tip thermal and mechanical hysteresis in Shape Memory Alloys under fatigue loading. *Materials Science and Engineering A*, *616*, 281–287.

Mutlu, F., Anlaş, G., & Moumni, Z. (2020). Effect of loading rate on fracture mechanics of NiTi SMA. *International Journal of Fracture*, *224*(2), 151–165.

Robertson, S.W., Mehta, A., Pelton, A.R., & Ritchie, R.O. (2007). Evolution of crack-tip transformation zones in superelastic Nitinol subjected to in situ fatigue: A fracture mechanics and synchrotron X-ray microdiffraction analysis. *Acta Materialia*, *55*(18), 6198–6207.

Roy, A.M. (2020). Influence of interfacial stress on microstructural evolution in NiAl alloys. *JETP Letters*, *112*(3), 173–179.

Shuai, J., & Xiao, Y. (2020). *In-situ* study on texture-dependent martensitic transformation and cyclic irreversibility of superelastic NiTi shape memory alloy. *Metallurgical and Materials Transactions A*, *51*(2), 562–567.

Ungár, T., Frenzel, J., Gollerthan, S., Ribárik, G., Balogh, L., & Eggeler, G. (2017). On the competition between the stress-induced formation of martensite and dislocation plasticity during crack propagation in pseudoelastic NiTi shape memory alloys. *Journal of Materials Research*, *32*(23), 4433–4442.

Xiao, Y., & Jiang, D. (2020a). Rate dependence of transformation pattern in superelastic NiTi tube. *Extreme Mechanics Letters*, *39*, 100819.

Xiao, Y., & Jiang, D. (2020b). Constitutive modelling of transformation pattern in superelastic NiTi shape memory alloy under cyclic loading. *International Journal of Mechanical Sciences*, *182*, 105743.

Xu, L., Solomou, A., Baxevanis, T., & Lagoudas, D.C. (2021). Finite strain constitutive modeling for shape memory alloys considering transformation-induced plasticity and two-way shape memory effect. *International Journal of Solids Structures*, *221*, 42–59.

You, Y., Gu, X., Zhang, Y., Moumni, Z., Anlaş, G., & Zhang, W. (2019). Effect of thermomechanical coupling on stress-induced martensitic transformation around the crack tip of edge cracked shape memory alloy. *International Journal of Fracture*, *216*(3), 123–133.

Yu, C., Kang, G., & Kan, Q. (2018). An equivalent local constitutive model for grain size dependent deformation of NiTi polycrystalline shape memory alloys. *International Journal of Mechanical Sciences*, *138–139*, 34–41.

Zhang, K., Kang, G., & Sun, Q. (2019). High fatigue life and cooling efficiency of NiTi shape memory alloy under cyclic compression. *Scripta Materialia*, *159*, 62–67.